

Frictional properties and 3-D stress analysis of the southern Alpine Fault, New Zealand

Carolyn Boulton^{a,b,*}, Nicolas C. Barth^c, Diane E. Moore^d, David A. Lockner^d, John Townend^a, Daniel R. Faulkner^b

^a School of Geography, Environment & Earth Sciences, Victoria University of Wellington, PO Box 600, Wellington, 6040, New Zealand

^b School of Environmental Sciences, University of Liverpool, Liverpool, L69 3GP, United Kingdom

^c Department of Earth Sciences, University of California, Riverside, CA, 92521, USA

^d U.S. Geological Survey, 345 Middlefield Road MS/977, Menlo Park, CA, 94025, USA

ABSTRACT

New Zealand's Alpine Fault (AF) ruptures quasi-periodically in large-magnitude earthquakes. Paleoseismological evidence suggests that about half of all recognized AF earthquakes terminated at the boundary between the Central and South Westland sections of the fault. There, fault geometry and the polarity of uplift change. The South Westland AF exhibits oblique-normal fault motion on a structure oriented 052°/82°SE that, for at least 35 km along strike, contains saponite-rich principal slip zone gouges. New hydrothermal friction experiments reveal that the saponite fault gouge is frictionally weak, exhibiting friction coefficients between $\mu = 0.12$ and $\mu = 0.16$ for a range of temperatures ($T = 25\text{--}210^\circ\text{C}$) and effective normal stresses ($\sigma_n' = 31.2\text{--}93.6$ MPa). The saponite gouge is rate-strengthening in all velocity steps performed at velocities between 0.01 and 3.0 $\mu\text{m/s}$, behavior conducive to aseismic creep. A three-dimensional stress analysis shows that the South Westland AF is favorably oriented with respect to the regional stress field for slip within the frictionally weak saponite fault gouge. Geometrically, the fault is severely misoriented for slip in any fault-forming materials with friction coefficients exceeding $\mu \sim 0.5$. The combination of weak gouges prone to aseismic creep, strong asperities, and low resolved shear stress may impede earthquake rupture propagation along the South Westland Alpine Fault.

1. Introduction

The Alpine Fault (AF) is a mature, ~ 850 km-long continental transform fault that poses the largest recognized onshore seismic hazard in New Zealand (Fig. 1) (Stirling et al., 2012). In conjunction with the Marlborough Fault System in the northern South Island, the Alpine Fault links two trenches dipping in opposite directions: the Hikurangi to the north, and the Puysegur to the south. Since its inception at approximately 25 Ma, the Alpine Fault has accrued over 480 km of displacement (Wellman, 1953; Sutherland et al., 2000; Lamb et al., 2015). During the late Quaternary, the AF has accommodated up to 75% of the total relative Australian-Pacific plate boundary motion, with the NUVEL-1A plate motion vector being approximately 36 mm/yr parallel to and 10 mm/yr perpendicular to the central AF (Beavan et al., 1999; Norris and Cooper, 2001; DeMets et al., 1994). An 8000-year composite paleoseismic record shows that the southern Alpine Fault ruptures every 291 ± 23 years in large-magnitude (Mw 7–8) earthquakes with devastating effects on the mountainous, landslide-prone landscape

(Sutherland et al., 2007; Berryman et al., 2012; Howarth et al., 2012, 2016; 2018; Cochran et al., 2017). Since the last major surface-rupturing earthquake was in 1717 CE (Wells et al., 1999), the Alpine Fault is late in its seismic cycle.

Although its surface trace is remarkably straight on the scale of the South Island, the Alpine Fault can be subdivided into five sections from south to north based on geometric, kinematic, geomorphologic, structural, and seismic attributes: the Fiordland, South Westland, Central, North Westland, and Wairau sections (Evison, 1971; Berryman et al., 1992; Barth et al., 2013) (Fig. 1). The fault maintains a high dextral slip rate of ~ 28 mm/yr from its junction with the Hope Fault to its termination at the Puysegur Trench, a distance of 540 km (Fig. 1) (Norris and Cooper, 2001; Barnes et al., 2005; Barnes, 2009; Barth et al., 2014). However, how slip is accommodated, and how earthquake ruptures propagate along the AF, remain areas of active research.

Recent analyses of sites along the Alpine Fault reveal that despite its highly regular recurrence intervals (Howarth et al., 2018), the fault exhibits two distinct types of earthquake behavior: 52% of the events

* Corresponding author. School of Geography, Environment & Earth Sciences, Victoria University of Wellington, PO Box 600, Wellington, 6040, New Zealand.

E-mail addresses: carolyn.boulton@vuw.ac.nz (C. Boulton), nic.barth@ucr.edu (N.C. Barth), dmoore@usgs.gov (D.E. Moore), dlockner@usgs.gov (D.A. Lockner), john.townend@vuw.ac.nz (J. Townend), faulkner@liverpool.ac.uk (D.R. Faulkner).

<https://doi.org/10.1016/j.jsg.2018.06.003>

Received 5 February 2018; Received in revised form 31 May 2018; Accepted 1 June 2018

Available online 18 June 2018

0191-8141/© 2018 Published by Elsevier Ltd.

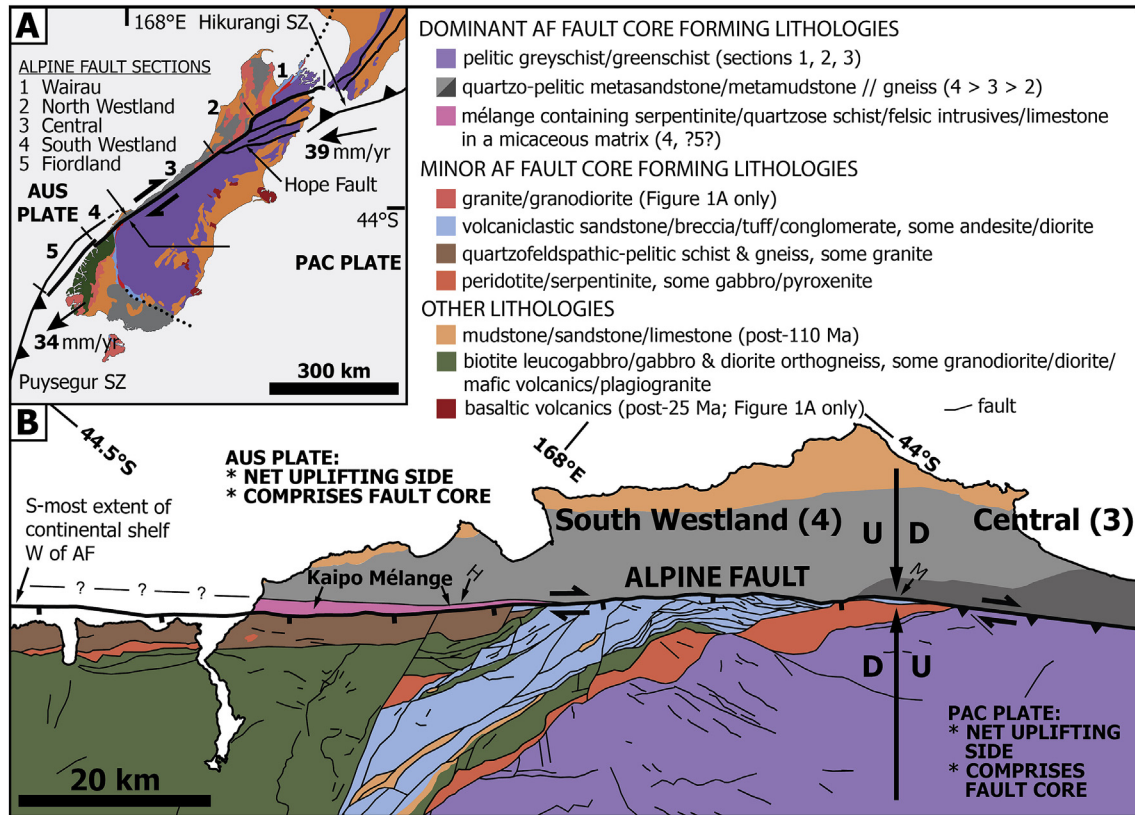


Fig. 1. Setting. (A) Simplified lithologic map of the South Island of New Zealand highlighting the five main fault sections. (B) Simplified lithologic map spanning the boundary between the Central and South Westland sections of the Alpine Fault. Note the switch in uplift polarity at the section boundary, which affects what materials comprise the fault core as exposed at the surface. Notice also the potential offshore extent of the serpentinite-bearing Kaipo Mélange. Abbreviations used: AUS (Australian), PAC (Pacific), AF (Alpine Fault), M (Marytr River), H (Hokuri Creek), SZ (subduction zone), U (up), D (down), S (South), W (West). Maps simplified after Barth et al. (2013).

are restricted to either the South Westland section (hereafter, the southern Alpine Fault) or the Central section (hereafter, the central Alpine Fault), and 48% of the events rupture both sections at the same time (Howarth et al., 2016, 2018; Cochran et al., 2017). The last three paleoearthquakes have been larger multi-section ruptures with a more variable sequence of single- and multi-section ruptures preceding them, making any temporal trend ambiguous (Howarth et al., 2018). Estimating the magnitude and spatial extent of the next AF earthquake may therefore require an understanding of how geometrical and lithological heterogeneity, as well as prior earthquake history, affect rupture nucleation, propagation, and arrest (Harris, 2004).

Geometrical heterogeneity may play a key role in governing the fault's variable rupture behavior (King, 1986; Wesnousky, 1988). The central-southern AF section boundary at the Martyr River is characterized by a distinct change in fault-zone architecture (Berryman et al., 1992; Barth et al., 2013). At this boundary, fault-zone orientation and kinematics change from dextral-reverse fault motion on the 45–55°SE-dipping, 055°-striking, central AF to dextral-normal fault motion on the 82°SE-dipping, 052°-striking, southern AF (Barth et al., 2013) (Fig. 1). The southern AF has long-term average Australian Plate uplift rates on the order of 2.6 mm/yr, compared with Pacific Plate uplift rates peaking at 6–9 mm/yr on the dextral-reverse central AF (Barth et al., 2013 and references within; Beavan et al., 2010). The orientation of the principal stresses is consistent across most of the South Island (Leitner et al., 2001; Townend et al., 2012; Boese et al., 2012, 2013). At depth, the central Alpine Fault is favorably oriented for slip in 'Byerlee' materials (with a friction coefficient, μ , around 0.6) if the magnitude of the least principal stress is similar to the intermediate principal stress, as commonly occurs on oblique reverse structures (Bott, 1959; Boulton, 2013; see also Supporting Information; Upton

et al., 2018). The extent to which the southern Alpine Fault is well oriented for slip, and what impact variations in fault geometry might have on seismic behavior, have not yet been explored.

The frictional properties of fault core lithologies may also influence seismic behavior (e.g., Titus et al., 2006; Faulkner et al., 2010; Kaneko et al., 2010; Jolivet et al., 2015). Whereas central AF fault rocks form from quartzofeldspathic, and rarely metabasic, schist and exhibit relatively little along-strike lithological variation (e.g., Norris and Cooper, 2007), southern AF fault rocks are derived from multiple protoliths ranging from ultramafics to metasediments and granitoids (Barth et al., 2013). Low-permeability, clay-rich fault gouges comprise the plate-boundary principal slip surface (PSS) along both the central and southern Alpine Fault (Boulton et al., 2012, 2017a; Barth et al., 2013). Southern AF gouges, however, contain saponite and are frictionally weaker than their central Alpine Fault counterparts (Boulton et al., 2012, 2014; 2017a; Barth et al., 2013). In this study, we evaluate what role the frictional properties of saponite fault gouges, in combination with the fault's distinctive geometry, might have on the mechanics of faulting along the southern AF. Our analysis combines four new hydrothermal friction experiments performed on the saponite fault gouge with a stress analysis and discussion of whether the southern Alpine Fault must necessarily have low frictional strength given its orientation.

2. Hydrothermal friction experiments

2.1. Material

Hydrothermal friction experiments were performed on a sample of saponite fault gouge collected from Hokuri Creek, where a 12 m-wide fault core contains clasts and pods of serpentinized peridotites

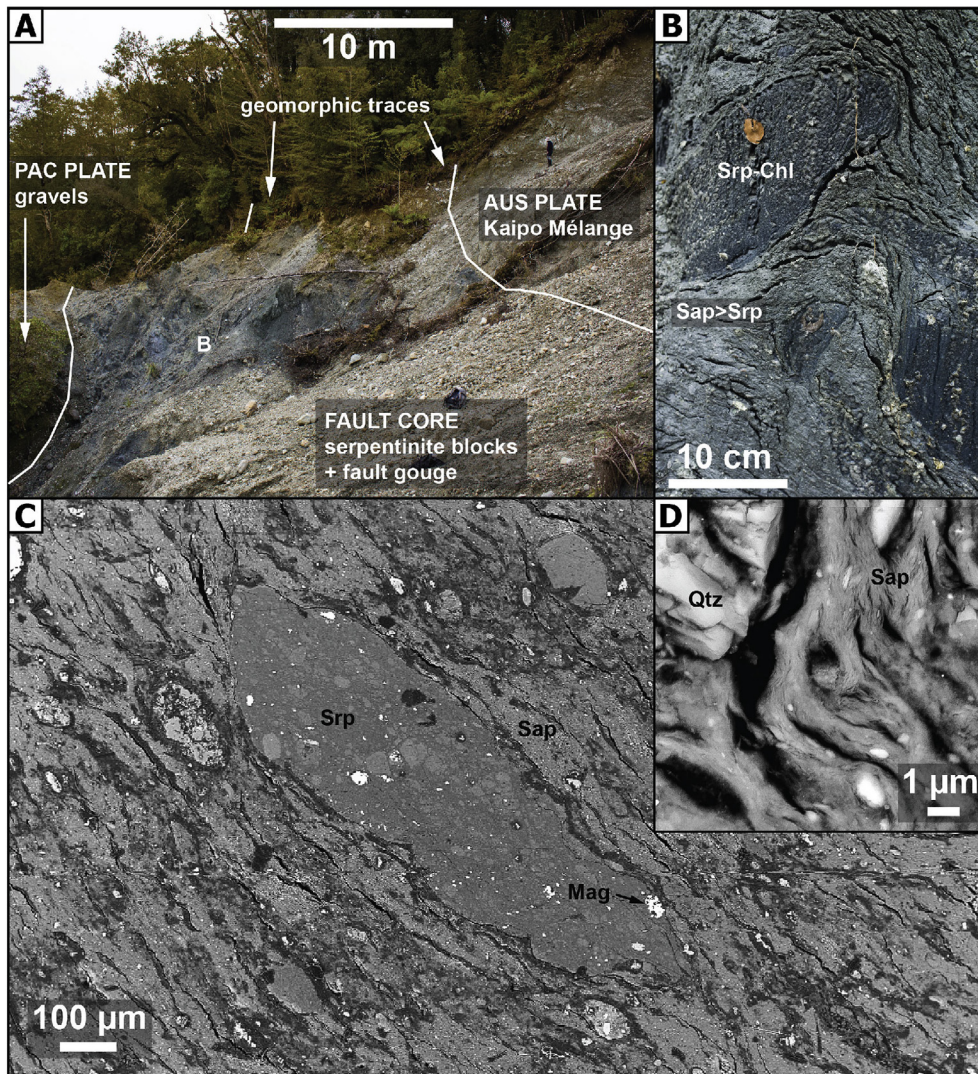


Fig. 2. Outcrop to SEM. (A) Exposure of Alpine Fault core at Hokuri Creek. (B) Close-up of outcrop in A showing deforming clasts of serpentinite-chlorite and foliated saponite gouge matrix (the latter was used in experiments). (C) Angle-selective backscatter SEM image of foliated saponite gouge sample. (D) High-magnification angle-selective backscatter SEM image showing the saponite matrix. The saponite occurs as continuous sheets that anastomose around clasts and define a high-vorticity foliation. Same sample as C. Darkest bands in B, C, and D are desiccation cracks that approximate the principal clay fabric. At all scales, the gouge is matrix-supported.

surrounded by a foliated fault gouge containing abundant saponite, an Mg-rich trioctahedral smectite formed by serpentinite alteration (Fig. 2A). The fault core lies between the Australian Plate Kaipo Mélange and Pacific Plate Quaternary sediments (Barth et al., 2013). Quantitative X-ray diffraction (XRD) analysis shows that the gouge contains the following constituents: saponite (74%), serpentinite (lizardite) (12%), calcite (5%), chlorite (3%), quartz (2%), talc (2%), and amphibole (actinolite) (2%) (Barth et al., 2013). The $< 2 \mu\text{m}$ separate contains saponite (78%), serpentinite (lizardite) (21%), and talc (1%), indicating that the bulk gouge is primarily neoformed saponite (Boulton et al., 2017a) (Fig. 2B). Detailed thin-section and SEM microstructural observations indicate that the saponite gouge has formed entirely within the Kaipo Mélange by the alteration of mafic clasts and serpentinite (Barth et al., 2013) (Fig. 2C and D). The minimum along-strike extent of the Kaipo Mélange is approximately 35 km, or $\sim 22\%$ of the total length of the 160 km-long southern AF section; because the fault strikes offshore, there is no clear constraint on the maximum extent of the mélangé. Southwest-to-northeast along-strike gradients in the competency of the Kaipo Mélange matrix, from incohesive to cohesive, and in carbonate clast lithology, from limestone to marble, suggests that the deformation within the mélangé occurred at upper to mid-crustal depths (Barth et al., 2013).

2.2. Experimental procedure

Prior to the friction experiments, the saponite gouge sample was dried overnight at 40°C , gently disaggregated using a mortar and pestle, and then sieved to obtain a $< 150 \mu\text{m}$ separate. A total of four shearing experiments were performed in a triaxial deformation apparatus at the U.S. Geological Survey in Menlo Park, California. Three experiments involved pressures and temperatures corresponding to a lithostatic confining pressure gradient consistent with a crustal density of 2650 kg/m^3 , hydrostatic pore fluid pressure, and a 35°C/km geothermal gradient; these conditions were used to match those of previous experiments on central Alpine Fault gouges (Boulton et al., 2014), although the limited data available suggest that the geothermal gradient is lower on the southern AF (Townend, 1999). One additional experiment was performed at room temperature and an effective normal stress of 31.2 MPa to provide data comparable with those obtained in previous experiments on central AF borehole gouges and surface outcrop gouges (Boulton et al., 2012, 2014). Thus, effective normal stress conditions ranged from 31.2 MPa to 93.6 MPa , and temperatures ranged from 25°C to 210°C (Table 1).

Experiments were conducted on a 1 mm-thick viscous gouge paste applied to a 30° inclined plane cut in a 19.1 mm-diameter granite cylinder. Sawcut surfaces were roughened with 120 grit SiC to avoid boundary slippage. Deionized water was used as pore fluid; pore fluid access to the fault was provided by a 2.4 mm-diameter line and constant

Table 1

List of experiments performed on the southern Alpine Fault saponite gouge. T is temperature in °C, σ_n' is effective normal stress in MPa, μ is coefficient of friction measured at a velocity of 0.1 $\mu\text{m/s}$ and 2.70 mm axial displacement. The friction rate parameter, a – b , listed is for the 0.1–1 $\mu\text{m/s}$ velocity step between 1.8 mm and 2.3 mm axial displacement.

Experiment	T (°C)	σ_n' (MPa)	μ	(a – b)
AFHT26	140	62.4	0.16	0.005
AFHT27	70	31.2	0.12	0.005
AFHT28	25	31.2	0.16	0.005
AFHT29	210	93.6	0.15	0.003

pressure was maintained. Servo-controlled confining pressure was adjusted once per second in response to changes in axial load to maintain constant normal stress on the inclined sawcut. Temperature measured inside the sample reached equilibrium within 30 min, and temperature varied by less than 2 °C during each experiment. To determine the friction rate parameter (a – b), velocity steps between 0.01 and 3 $\mu\text{m/s}$ were imposed (equivalent to strain rates of 0.01–3 s^{-1} if slip is distributed across the 1 mm-thick gouge layer). Samples were sheared for a total axial displacement of 3.6 mm, resulting in a net fault-parallel displacement of 4.14 mm.

Corrections were made for seal friction, the pressure- and velocity-dependence of seal friction, changes in contact area of the sawcut surfaces, elastic deformation of the loading system, Teflon shim friction, and the temperature-dependent shear resistance of the lead jackets used. Typical uncertainties in the coefficient of friction reported for experiments performed using lead jackets are ± 0.02 , and the shear resistance of the lead jackets is insensitive to velocity. The experimental configuration is portrayed in Fig. 3, and experimental methods and corrections are described in full by Moore and Lockner (2011).

2.3. Data analysis

Strength results are presented in terms of the coefficient of (sliding) friction, $\mu = \tau/\sigma_n'$ where τ is the resolved shear stress, $\sigma_n' = \sigma_n - P_p$ is the effective normal stress, and σ_n and P_p are the resolved normal stress and pore pressure, respectively. For each experiment, the reported coefficient of friction was measured at a velocity of 0.1 $\mu\text{m/s}$ after 2.70 mm of axial displacement. Linear stability analyses show that the mechanical conditions and constitutive properties that distinguish stable (aseismic) from unstable (seismic) sliding can be quantified by the friction rate parameter (a – b) and the critical slip distance d_c (Dieterich, 1979; Ruina, 1983). In the Dieterich (1979) rate-and-state friction equation:

$$\mu_{ss} = \mu_0 + a \ln\left(\frac{V}{V_0}\right) + b \ln\left(\frac{V_0 \theta}{d_c}\right) \quad (1)$$

Here, V_0 and V are the initial and final load point velocities, respectively, μ_0 and μ_{ss} are the initial and final, steady-state, friction coefficients, a and b are empirical constants, and θ is a state variable that evolves with time according to:

$$\frac{d\theta}{dt} = 1 - \frac{V\theta}{d_c} \quad (2)$$

When a – $b > 0$, the material is rate-strengthening and frictional sliding will be stable. When a – $b < 0$, the material is rate-weakening and frictional sliding will be unstable, or potentially unstable. For unstable slip to occur, the elastic stiffness, k , of the loading system must also be less than the critical stiffness, k_c , which is defined by the frictional properties of the slipping fault (Ruina, 1983). For each velocity step, the friction rate parameter (a – b) was determined with the Xlook program using the Dieterich (1979) equation and the inversion technique described by Saffer and Marone (2003).

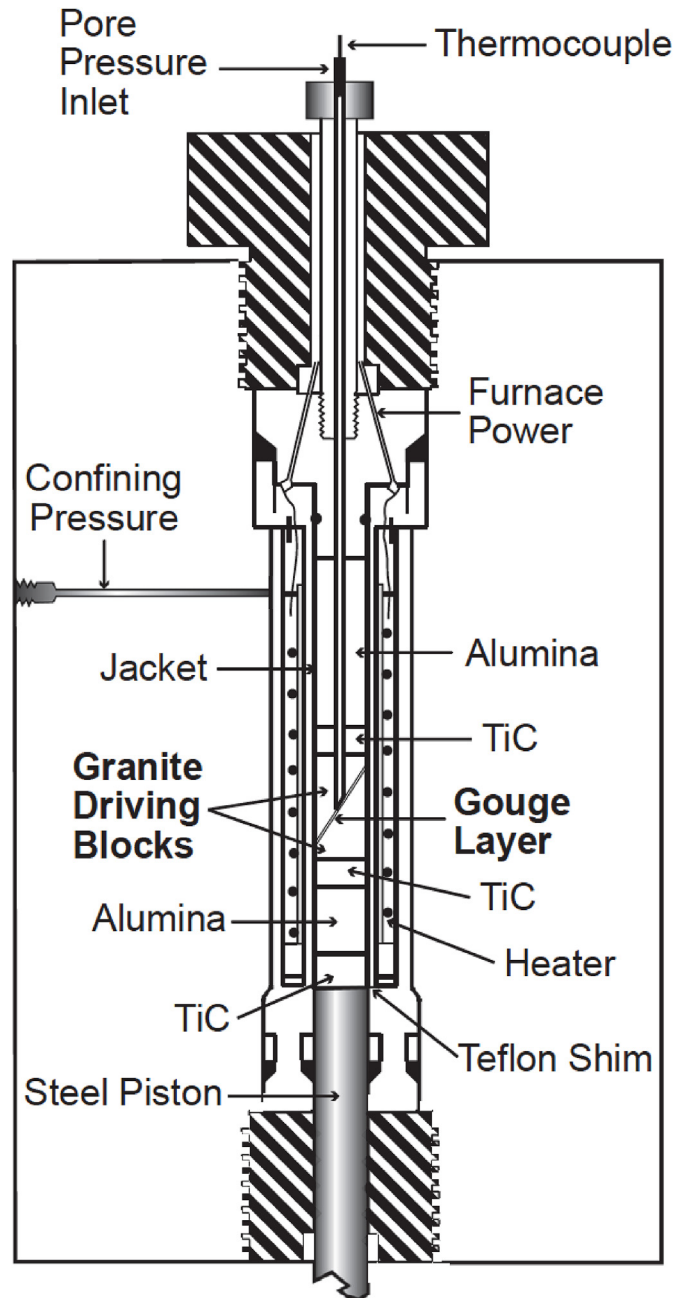


Fig. 3. Experimental assembly used for the triaxial friction experiments (Moore et al., 2016).

2.4. Experimental results

The complete results of each experiment are plotted as coefficient of friction against displacement in Fig. 4. The frictional behavior is approximately independent of effective normal stress and temperature. Once steady-state behavior is reached at approximately 1.5 mm axial displacement, all friction coefficient data fall in the range of 0.12–0.16 (Table 1). Thus, the coefficient of friction for the saponite gouge was determined by fitting a line to a plot of the shear stress vs normal stress data collected during the four new friction experiments and the low normal-stress room-temperature experiment reported in Barth et al. (2013). The slope yields a coefficient of friction of $\mu = 0.15$ (Fig. 5).

Values of (a – b) are uniformly positive, indicating that the southern AF saponite gouge is rate-strengthening for all temperatures, pressures, and velocities tested (Fig. 6a). Repeat steps with a final sliding velocity

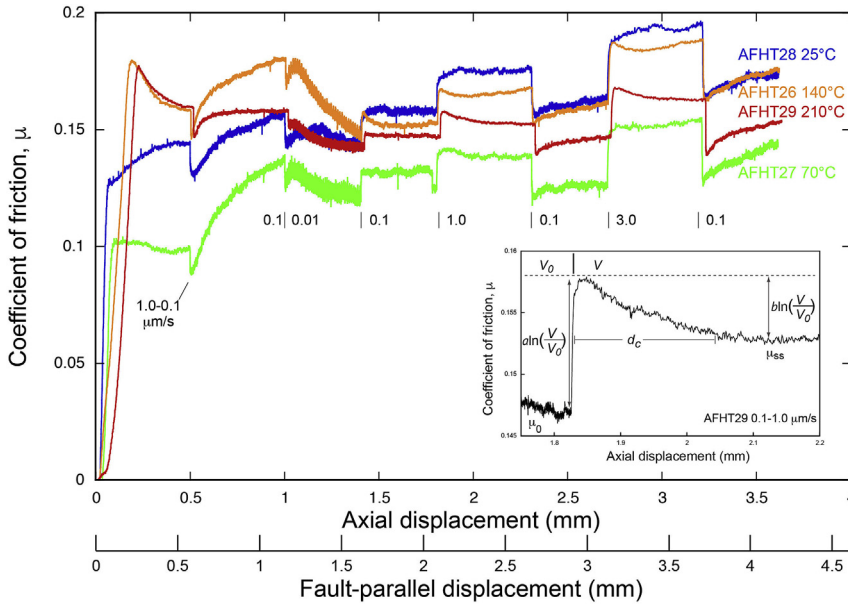


Fig. 4. Plot of coefficient of friction vs. axial displacement for triaxial experiments conducted on southern Alpine Fault saponite gouge. As shown, fault-parallel displacement is approximately 15% larger than axial displacement. The displacements at which velocity steps occurred are demarcated, along with the velocity imposed. Rate-and-state friction parameters are depicted on the inset figure, an enlargement of the 0.1–1.0 $\mu\text{m/s}$ velocity step in AFHT29, performed at $T = 210^\circ\text{C}$ and $\sigma'_n = 93.6\text{ MPa}$.

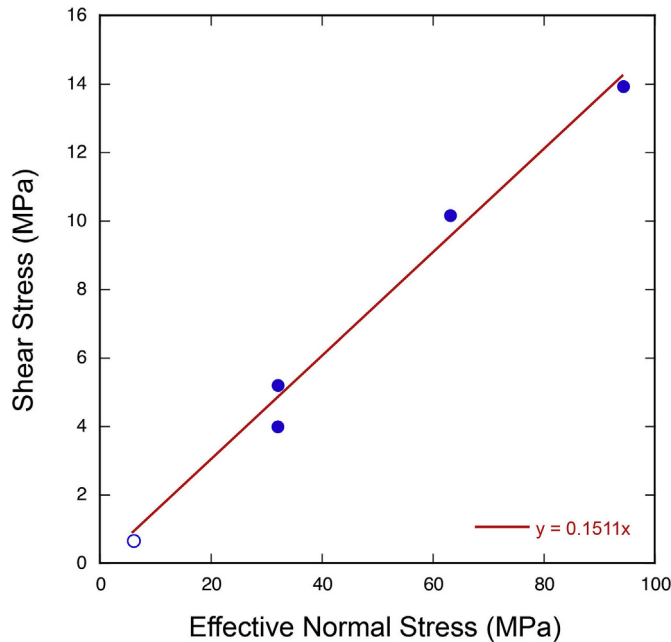


Fig. 5. A plot of shear stress (τ), measured at 2.70 mm axial displacement, against effective normal stress (σ'_n) for all friction experiments performed on the southern Alpine Fault saponite gouge. Closed circles denote experiments performed in the triaxial apparatus in this study, and open circle denotes an experiment performed in a double-direct shear apparatus on an intact sample and published previously in Barth et al. (2013). Regression line has been forced through the origin; the line with the smallest residual has a slope (μ) of 0.1538 and results in a negative value of cohesion (-0.175 MPa).

(V) of $0.1\ \mu\text{m/s}$ show a trend towards increasing values of $a-b$ with displacement due to factors that may include shear-enhanced compaction, grain size reduction, and/or microstructural development (e.g., Morrow et al., 2017; Faulkner et al., 2018) (Fig. 6b). The repetition of the $0.1\ \mu\text{m/s}$ velocity step also shows that the experiments performed at the lowest temperature and effective normal stress, AFHT 28, displayed a strain-hardening trend (Fig. 4).

3. Southern Alpine Fault stress analysis

The experimental results above show that saponite gouges along the southern Alpine Fault are frictionally weak across a broad range of temperatures and pressures (Table 1) (Figs. 4 and 5). Here, we explore the extent to which frictional weakness is required for slip on the southern AF. The Mohr-Coulomb theory forms the basis of this analysis and specifies that frictional failure will occur when:

$$\tau = C_0 + \mu_i(\sigma'_n) = C_0 + \mu_i(\sigma_n - P_p) \quad (3)$$

That is, a fault will move when shear stress (τ) is equal to cohesion (C_0) plus the product of the internal friction coefficient (μ_i) and the effective normal stress ($\sigma'_n = \sigma_n - P_p$). For existing faults, cohesion is assumed to be negligible, and the equation reduces to:

$$\tau = \mu_s(\sigma_n - P_p) \quad (4)$$

where (μ_s) is the static coefficient of friction (cf. Fig. 5). This analysis stipulates that frictional slip will occur when the stress state on a fault intersects the Mohr-Coulomb failure envelope (Fig. 7). In a 2-dimensional stress analysis, the magnitude of shear stress (τ) acting on the fault depends on the orientation of the fault plane as well as the orientation of the maximum ($\sigma_1 = S_{Hmax}$) and minimum ($\sigma_3 = S_{Hmin}$) principal stresses (Sibson, 1985). In three dimensions, the shear stress and normal stress acting on a fault plane can be calculated using Cauchy's equations (Jaeger et al., 2007):

$$\tau^2 = (\sigma_1 - \sigma_2)^2 l^2 m^2 + (\sigma_2 - \sigma_3)^2 m^2 n^2 + (\sigma_3 - \sigma_1)^2 l^2 n^2 \quad (5)$$

and

$$\sigma_n = l^2 \sigma_1 + m^2 \sigma_2 + n^2 \sigma_3 \quad (6)$$

where l , m , and n denote the direction cosines between the pole to the fault plane and the maximum, σ_1 , intermediate, σ_2 , and minimum, σ_3 , principal stresses, respectively (and $\sigma_1 \geq \sigma_2 \geq \sigma_3$; Fig. 7). The orientations of the principal stresses acting on the central Alpine Fault have been determined from focal mechanism inversions of hanging wall seismicity to be $\sigma_1 = S_{Hmax} = 0/117^\circ$, $\sigma_2 = \sigma_v$, and $\sigma_3 = S_{Hmin} = 0/207^\circ$ (Boese et al., 2012, 2013; see also the work of Warren-Smith et al., 2017a, 2017b who reported that $\sigma_1 = S_{Hmax} = 114 \pm 10^\circ$ along the central-to-southern AF and Townend et al., 2012, who showed that a similar S_{Hmax} orientation prevails across most of the South Island). If the mean orientation of the upper, brittle, southern AF is assumed to be parallel to the surface measurements of the fault plane, $052^\circ/82^\circ\text{SE}$

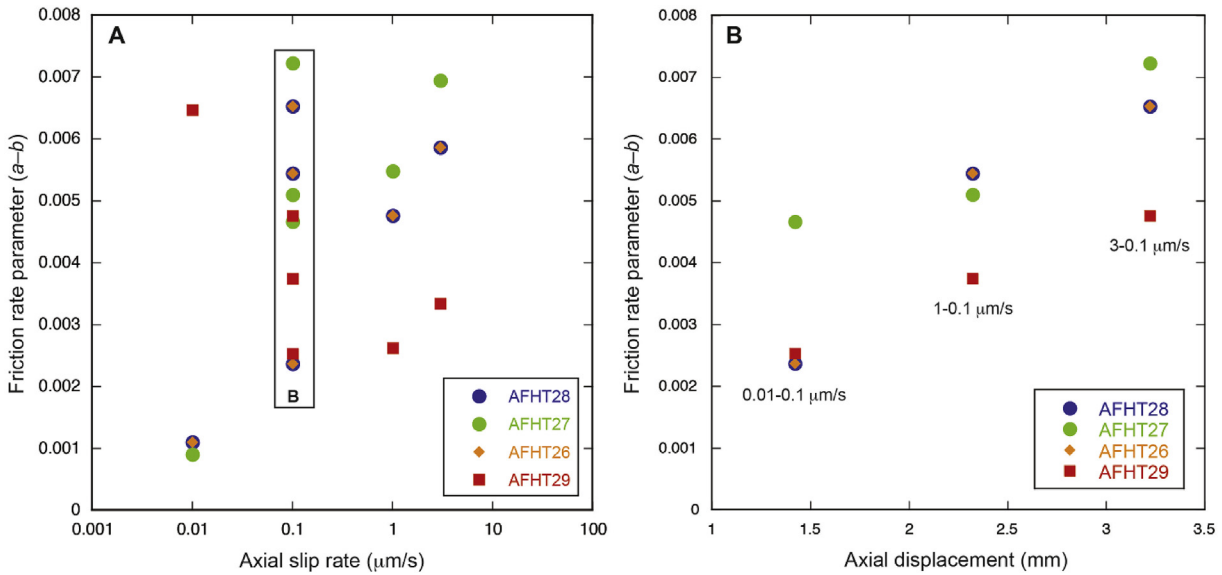


Fig. 6. Summary plot of the friction rate parameter, $a-b$, determined by modelling velocity steps. All velocity steps are rate-strengthening. Experimental conditions are listed in Table 1, and colors correspond to the complete experimental data plotted in Fig. 4. (A) Plot of friction rate parameter against axial slip rate, showing a range of values for velocity steps with a final sliding velocity (V) of $0.1 \mu\text{m/s}$ (boxed), which are shown in (B) to be displacement (and/or time) dependent (see text for details). (For interpretation of the references to color in this figure legend, the reader is referred to the Web version of this article.)

(corroborated in part by the offshore seismic reflection studies of Barnes et al., 2005), the plane does not contain the intermediate principal stress (σ_2) (inset, Fig. 7). Thus, a 3-D stress analysis is necessary to determine whether the fault is favorably oriented for slip (e.g. Sibson, 1985).

3.1. 3-D stress analysis methods

We used the 3-D stress analysis developed by Leclère and Fabbri (2013) to evaluate whether frictional weakness is required for slip on the southern Alpine Fault. The method is summarized below and all analyses were performed using Matlab. The Leclère and Fabbri (2013) method builds on the slip-tendency analysis of Morris et al. (1996) by

incorporating the orientations of all three principal stresses and identifying the conditions where slip is only possible when pore fluid pressure is greater than the least principal stress (see also Nevis et al., 2009). The shear stress and normal stress resolved on the southern AF were computed after Jaeger et al. (2007), assuming that the orientation of the three principal stresses is equal to the seismologically determined stress regime, and that the fault plane is parallel to the surface trace of the southern AF (Equations (5) and (6)) (Boese et al., 2012; Barth et al., 2013). The relative magnitudes were quantified by assuming a stress shape ratio Φ :

$$\Phi = (\sigma_2 - \sigma_3) / (\sigma_1 - \sigma_3) \tag{7}$$

While these assumptions remain simplistic, there are no *in situ*

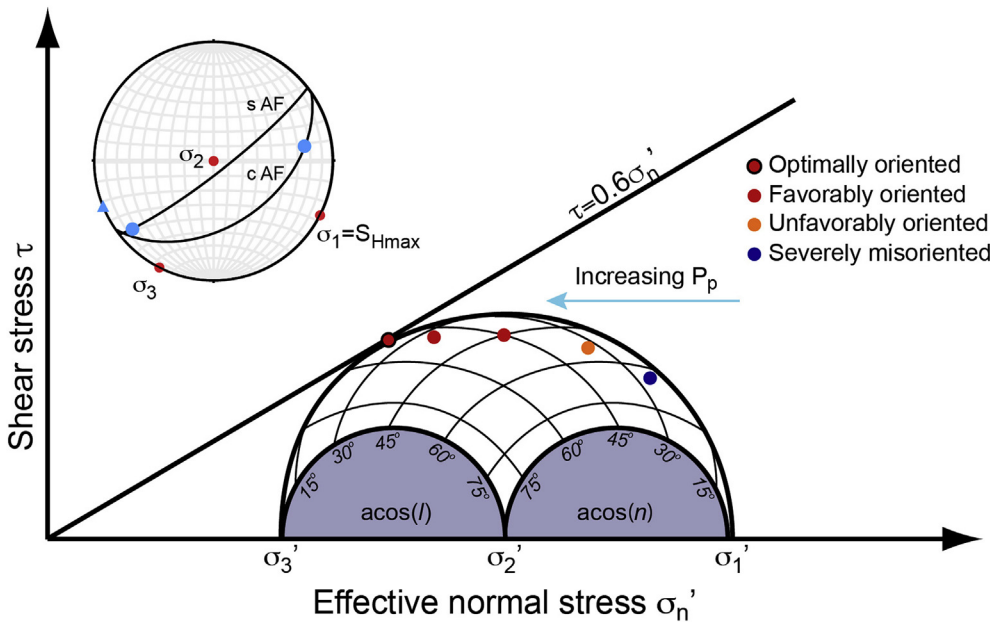


Fig. 7. A Mohr diagram showing the re-shear criterion for a typical 'Byerlee' friction value of $\mu = 0.6$. The Mohr circles are drawn for a stress shape ratio (Φ) of 0.5. In the inner circles, acos stands for inverse cosine function, used to compute the magnitudes of shear stress and effective normal stress resolved on the fault plane following Jaeger et al. (2007), where l is the angle between σ_1 and the pole to the fault. The angle between σ_3 and the pole to the fault is n . The orientations of four representative fault planes are shown: one optimally oriented (red circle), one favorably oriented (orange circle), one unfavorably oriented (green circle), and one severely misoriented (blue circle). The severely misoriented circle depicts the orientation of the southern Alpine Fault with respect to σ_1 . Increasing pore fluid pressure (P_p), or, alternatively, rotating σ_1 counterclockwise, increases the shear stress acting on the southern AF (R-L, green to red circles). The inset lower hemisphere equal area stereoplots shows the orientation of the central (c AF) and southern (s AF) Alpine Fault planes along with the slip vector on each fault section (blue circles), the NUVEL-1A plate vector calculated for Hokuri Creek (blue triangle), and the seismologically determined orientation of the three principal stresses (red circles) (after Barth et al., 2013; Boese et al., 2012, 2013; Townend et al., 2012). (For interpretation of the references to color in this figure legend, the reader is referred to the Web version of this article.)

southern (s AF) Alpine Fault planes along with the slip vector on each fault section (blue circles), the NUVEL-1A plate vector calculated for Hokuri Creek (blue triangle), and the seismologically determined orientation of the three principal stresses (red circles) (after Barth et al., 2013; Boese et al., 2012, 2013; Townend et al., 2012). (For interpretation of the references to color in this figure legend, the reader is referred to the Web version of this article.)

measurements of the orientation or magnitude of the principal stresses acting at depth on any section of the Alpine Fault (e.g., Townend et al., 2009, 2017; Massiot et al., 2018). For the assumed stress regime, fault plane orientation, stress shape ratio, and coefficient of friction, an effective stress ratio, Q , required for slip was determined, whereby:

$$Q = (\sigma'_3)/(\sigma'_1) \quad (8)$$

The prime (') here denotes the magnitude of the effective principal stress (Leclère and Fabbri, 2013). If $\sigma'_1 = \sigma'_3$, $Q = Q_{\max} = 1$. The magnitude of the effective intermediate and minimum principal stresses, σ'_2 and σ'_3 , and thus the dimensions of the 3-D Mohr circle, were found using the stress shape ratio Φ (Equation (7)), the effective stress ratio Q (Equation (8)), and substitution:

$$\sigma'_2 = \sigma'_1[\Phi(1 - Q) + Q] \quad (9)$$

and

$$\sigma'_3 = \sigma'_1 Q \quad (10)$$

The magnitudes of the effective principal stresses were then substituted into equations (5) and (6), allowing Q to be calculated for any given static coefficient of friction (see full analytical method used in solving for Q in Leclère and Fabbri, 2013). Where θ_r^* is the optimal angle for slip (Sibson, 1985), the optimal effective stress ratio (Q_{optimal}) is equal to:

$$Q_{\text{optimal}} = (1 - \mu_s \tan \theta_r^*) / (1 + \mu_s \cot \theta_r^*) \quad (11)$$

and

$$\theta_r^* = \frac{1}{2} \tan^{-1}(1/\mu_s) \quad (12)$$

Thus, the optimal effective stress ratio depends on the static coefficient of friction (see also Supplementary Fig. 1B) (Leclère and Fabbri, 2013; Leclère et al., 2013) (Fig. 7). Following Byerlee (1978), we equate the static coefficient of friction (μ_s) with the coefficient of friction (μ) measured experimentally (above, Section 2).

3.2. 3-D stress analysis results

The southern Alpine Fault is favorably oriented for frictional failure in weak saponite gouges ($\mu = 0.15$) (Fig. 8), but not in stronger materials with Byerlee-type friction coefficients ($\mu \sim 0.6$) (Fig. 8). In fact, for a stress shape ratio typical of a strike-slip fault, $\Phi = 0.50$ (Bott, 1959; see also Boese, 2012), patches of the southern AF with Byerlee friction coefficients are severely misoriented for failure (Fig. 8). Because our hydrothermal friction experiments were conducted on saponite gouges that comprise a modest proportion of the total length of the southern

AF, the results are probably not applicable to the entire fault plane. Therefore, in Fig. 9 we present results of the 3-D stress analysis performed at every possible coefficient of friction and every possible stress shape ratio for the assumed fault plane orientation and stress regime. The results show that regardless of stress shape ratio, all values of Q are negative when the coefficient of friction is 0.5 or greater. That is, for the conditions analyzed, patches of the southern Alpine Fault that are frictionally stronger than $\mu \sim 0.5$ would require pore fluid pressures greater than the least principal stress for slip (Fig. 9).

4. Discussion

4.1. Occurrence and comparison with other saponite fault gouges

Sedimentological, geomorphological, and paleoseismological evidence indicates that slip is accommodated coseismically on the saponite-bearing portion of the fault at Hokuri Creek (Wells and Goff, 2007; Berryman et al., 2012; Clark et al., 2013; Howarth et al., 2016, 2018). Along the southern AF, saponite occurs solely within a single 1.1 m- to 12 m-wide fault core as the primary mineralogical constituent of a foliated fault gouge containing oblate clasts of serpentinite (lizardite \pm actinolite \pm talc \pm magnetite \pm chromite \pm calcite) along with minor amounts of schist (quartz + feldspar + muscovite + biotite) and pervasively hydrothermally altered mafic rocks (Barth et al., 2013) (Figs. 1 and 2). The serpentinite clasts commonly contain reaction rims of lizardite-chlorite, and it is inferred that the saponite formed from the low-temperature alteration of serpentinite in the presence of fluids containing both silicon and aluminum (Velde and Meunier, 2008; Barth et al., 2013). Because there are no age constraints on the formation of the foliated gouge, we cannot exclude the possibility that the fabric formed via postseismic and/or interseismic creep processes (cf. Holdsworth et al., 2011; Moore, 2014).

Similar saponite-rich foliated fault gouges were recovered from the creeping segment of the San Andreas Fault at 2.7 km vertical depth in SAFOD (the San Andrea Fault Observatory at Depth) (Bradbury et al., 2011; Lockner et al., 2011; Holdsworth et al., 2011; Moore, 2014; Moore et al., 2016). In the SAFOD borehole, saponite occurs within two actively creeping shear zones, the southwest deforming zone (SDZ) and the central deforming zone (CDZ); of the two, the CDZ is creeping more quickly and contains more clay (e.g., Lockner et al., 2011; Moore, 2014). Fault gouge containing saponite also occurs within the creeping segments of the North Anatolian Fault in Turkey and within the inactive Gokasho-Arashima tectonic line in Japan (Kaduri et al., 2017; Sone et al., 2012).

The friction coefficients measured during hydrothermal friction

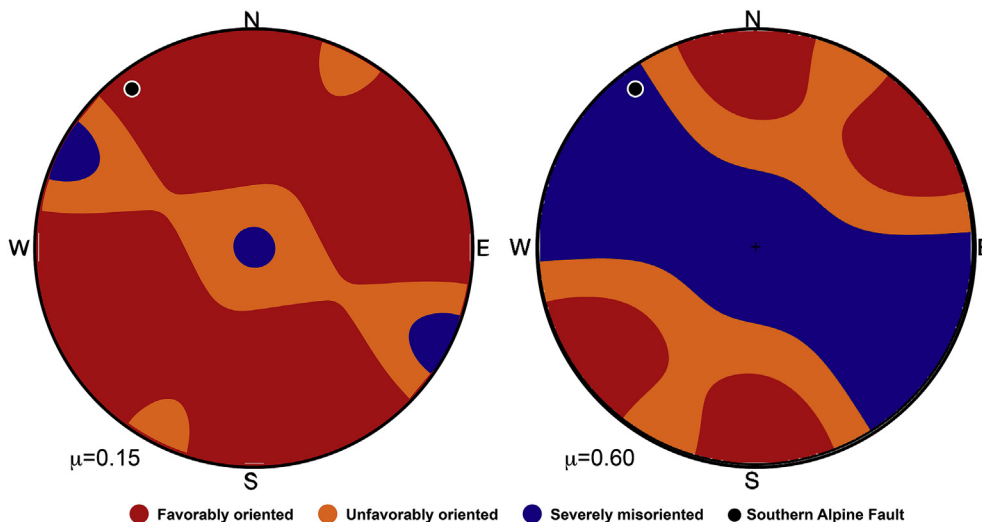


Fig. 8. Results of the 3-D reactivation analysis conducted on the southern Alpine Fault. The pole to the fault, oriented 052°/82°SE, is shown as a black circle outlined in white in the stereoplots. The colors within stereoplots are simply contoured to depict whether, given the input values of the seismologically determined orientation of the three principal stresses and a stress shape ratio (Φ) of 0.5, the orientation of a structure is favorable (red), unfavorable (orange), or severely misoriented (blue) for a coefficient of friction of $\mu = 0.15$ (left stereoplot) or $\mu = 0.6$ (right stereoplot). (For interpretation of the references to color in this figure legend, the reader is referred to the Web version of this article.)

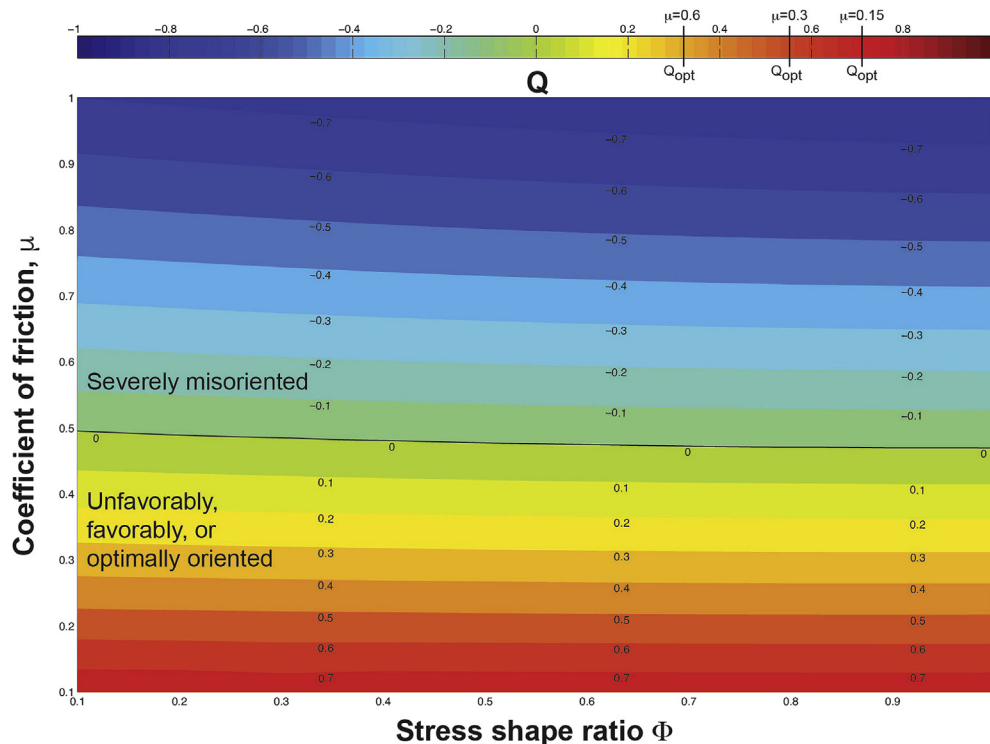


Fig. 9. A contour plot generated from Q values obtained in the 3-D reactivation analysis of the southern Alpine Fault. All stress shape ratios between 0.1 and 1.0, and all coefficients of friction between 0.1 and 1.0, were evaluated. The value of $Q_{optimal}$ for different friction coefficients is shown in the scale bar. The bold line on the contour plot corresponds to $Q = 0$. Unfavorably oriented fault planes have Q values between $2/3Q_{optimal}$ and 0. Negative values of Q indicate that faults with friction coefficients > 0.5 require pore fluid pressures greater than the least principal stress to slip.

experiments performed on southern Alpine Fault saponite gouge at 25–210 °C agree well with experimental results obtained at a range of temperatures on San Andreas Fault and Gokasho-Arashima tectonic line gouges (Lockner et al., 2011; Carpenter et al., 2012, 2015; Sone et al., 2012; Coble et al., 2014; French et al., 2015; Moore et al., 2016). Despite being performed on different deformation apparatus and at varying effective normal stresses and total shear strains, saturated saponite fault gouges are consistently very weak with friction coefficients between $\mu = 0.06$ and $\mu = 0.21$. Our results, $\mu = 0.12$ to $\mu = 0.16$, fall within this range. Unlike results obtained from CDZ gouge (~65% saponite plus 15–20% serpentine) (French et al., 2015; Moore et al., 2016), the southern Alpine Fault gouge (74% saponite plus 12% serpentine) did not weaken with increasing temperature in the experiments performed (Fig. 4). The southern AF gouge contains more saponite than the CDZ gouge, and the frictional strength of pure saponite has been shown to have no obvious temperature dependence up to 200 °C ($\mu = 0.04$ –0.08; Moore et al., 2016).

The velocity dependence of friction, as measured with the friction rate parameter a – b , indicates whether a fault-forming material is prone to stable, aseismic creep or unstable, seismic slip (e.g., Dieterich, 1979; Ruina, 1983). Across all velocities, temperatures, and effective normal stresses tested, the southern Alpine Fault gouge is rate-strengthening. Other experiments performed on saponite gouges within the velocity range at which earthquakes are thought to nucleate ($V < 0.1$ m/s) have yielded the same results (e.g., Lockner et al., 2011; Carpenter et al., 2012, 2015; Sone et al., 2012; Barth et al., 2013; Moore et al., 2016). The values of a – b reported here, between 0.001 and 0.010, are within the same range as those reported for powdered CDZ San Andreas Fault gouges in Moore et al. (2016) (Fig. 6). Slightly higher a – b values of up to 0.014 were obtained at low effective normal stress ($\sigma_n' = 7$ MPa) in experiments performed by Carpenter et al. (2015). The SDZ, which contains proportionately less saponite than the CDZ and southern Alpine Fault gouge, did exhibit rate-weakening behavior at the highest temperatures and lowest velocities imposed ($T = 200$ and 250 °C; $V = 0.001$ and 0.01 $\mu\text{m/s}$). It is likely that other minerals present within the SDZ gouge influence its behavior, as experimental results obtained from a pure saponite separate show consistent rate-

strengthening behavior (Moore et al., 2016).

Our results, taken in conjunction with previously published experimental data, indicate that the clay mineral saponite controls the frictional behavior of fault gouges when it forms the load-bearing matrix (Tembe et al., 2010; Moore et al., 2016). Therefore, understanding the thermodynamic stability of saponite is necessary to interpret experimental results and extrapolate them to *in situ* conditions. Saponite is a 2:1 layered 10 Å trioctahedral smectite mineral wherein all three sites around each hydroxyl ion in the octahedral layer are coordinated with a cation, usually divalent Mg^{2+} (Eberl et al., 1978). Trioctahedral saponite is relatively stable because mineral transformation is impeded by its fully coordinated octahedral layer and low aluminum concentration (Ames and Sand, 1958; for a detailed discussion, see Eberl et al., 1978). Thus, over short time periods, such as our laboratory friction experiments or a mineral synthesis reaction, saponite is stable at temperatures as high as 550–850 °C (e.g., Klopogge et al., 1999; Moore et al., 2016). However, over longer time scales, such as the life of a crustal-scale fault zone or sedimentary basin, saponite stability lies in the range of ~25–150 °C (Velde and Meunier, 2008). At temperatures above ~150 °C, saponite is replaced by corrensite and/or chlorite (Meunier, 2005; see also Schleicher et al., 2012; Moore, 2014). Chlorite is only present in trace amounts in the southern AF gouge studied here (3%), so if present in abundance at depth, retrograde transformation reactions have replaced it with saponite.

4.2. Comparison with central Alpine Fault gouges

The central Alpine Fault section strikes northeast for 250 km from the Martyr River to the Hope Fault (Fig. 1). Whereas the southern AF undergoes oblique-normal displacement, the central section is oblique-reverse and rapidly exhumes amphibolite-facies mylonites from ~35 km depth (Little et al., 2005). Along the central AF, a 1–10 cm-thick fault gouge derived from Pacific-Plate protoliths commonly occurs along the contact between Pacific Plate mylonites or cataclasites and Australian Plate gravels, granitoids, or metasediments (e.g., Cooper and Norris, 1994; Norris and Cooper, 2001, 2007; Barth et al., 2012; Boulton et al., 2012) (Fig. 1). Saponite has never been found on the

central AF; there, the dioctahedral smectite mineral montmorillonite comprises up to 36% of the plate-boundary fault gouge (Warr and Cox, 2001; Boulton et al., 2012, 2014; 2017a). The hydrothermal frictional properties of montmorillonite-bearing fault gouges recovered from shallow Deep Fault Drilling Project boreholes (DFDP-1) were measured by Boulton et al. (2014) and Niemeijer et al. (2016). Both studies found that a plate-boundary gouge containing montmorillonite (26%) strengthens markedly with increasing temperature. The coefficient of friction, measured at 2–3 mm displacement, increased from $\mu = 0.43\text{--}0.45$ at 20–25 °C to $\mu = 0.60\text{--}0.74$ at 210–300 °C. An increase in strength was found to coincide with the transition from rate-strengthening to rate-weakening, and in some cases stick-slip, behavior (Boulton et al., 2014; Niemeijer et al., 2016). In contrast, southern AF saponite gouges remained very weak and rate-strengthening throughout the temperature range 25–210 °C (Figs. 4 and 6).

To summarize the differences between central and southern Alpine Fault shallow, smectite gouges: (1) the absolute abundance of smectite minerals is greater within the southern AF gouge; (2) the smectite mineral present within the southern AF gouge, saponite, is weaker over the entire range of temperatures and pressures simulated experimentally; and (3) smectite is thermodynamically stable over a much larger depth range on the southern AF. As a consequence of along-strike differences in uplift rate and polarity on the AF, the central section has high heat flow, with measured geothermal gradients of 62.6 ± 2.1 °C/km and 125 ± 55 °C/km, and a microseismicity cut-off depth of 10 ± 2 km (Koons, 1987; Sutherland et al., 2012, 2017; Boese et al., 2012; Townend et al., 2017). In contrast, the dominant microseismicity cut-off depth is between 15 and 20 km near the southern AF, yielding a depth-averaged geothermal gradient of < 25 °C/km assuming the onset of quartz plasticity marks the frictional-viscous transition (Boese et al., 2012; Bourguignon et al., 2015; Warren-Smith et al., 2017b). Thus, fault gouge along the southern AF has had more time to undergo low-temperature saponite-forming reactions (on the order of 10^6 years, vs. 10^5 years on the central AF), and the maximum depth of smectitic, rate-strengthening fault gouge on the southern AF is ~ 6 km, as opposed to ~ 2 km or less on the central Alpine Fault (Boulton et al., 2012; Boles et al., 2018).

4.3. Implications for slip on the southern Alpine Fault

In the 3-D stress analysis presented in Section 3, the effective stress ratio, Q , required for reactivation of the southern Alpine Fault was computed for different friction coefficients based on the fault's orientation, the seismologically determined orientation of the three principal stresses, and the relative magnitudes of the principal stresses (Figs. 7–9) (Leclère and Fabbri, 2013). The analysis showed that reactivation, via earthquake nucleation or aseismic creep, is potentially favorable for fault rocks with friction coefficients less than 0.5. For any ratio of the principal stresses (stress shape ratio), the southern AF is favorably oriented for frictional sliding of the saponite fault gouge, which has a coefficient of friction of 0.15 (Figs. 8 and 9). However, regardless of the relative magnitudes of the principal stresses (stress shape ratio), the southern Alpine Fault is severely misoriented for frictional failure of fault rocks with friction coefficients exceeding ~ 0.5 , requiring pore-fluid overpressures greater than the least principal stress ($P_p > \sigma_3$) (Fig. 9). A correlation exists between rate-weakening behavior and frictional strength in montmorillonite gouge, chlorite-white mica gouge, cataclases, and ultramylonites on the central AF: rate-weakening behavior occurs when the coefficient of friction is greater than $\mu \sim 0.6$ (Boulton et al., 2014; Ikari et al., 2015; Niemeijer et al., 2016). Insufficient driving stress exists on the southern AF to exceed the frictional strength of similar materials without pore-fluid overpressures.

The stress analysis does not yield the absolute value of pore fluid pressure required for failure of frictionally strong gouges. Several additional assumptions are needed to quantify the pore fluid pressure,

including the absolute magnitude of at least one principal stress, the increase in differential stress with depth, the coefficient of friction of any frictionally strong rocks, and the depth at which the frictionally strong rocks occur. It is likely, for a strike-slip fault, that the intermediate principal stress (σ_2) is equal to the overburden pressure (Anderson, 1905). However, the differential stress acting on any section of the AF has never been measured *in situ*, and quantifying it remains an outstanding goal of the Deep Fault Drilling Project (Townend et al., 2009). Furthermore, no comprehensive geophysical and/or field data exist on the distribution and frictional strength of fault rocks comprising the lithologically heterogeneous southern AF principal slip zone (Barth et al., 2013; this study). Thus, further quantification of the state of stress and pore fluid pressures acting within the southern AF is outside the scope of this study. It is sufficient to note that pore fluid pressures greater than the least principal stress are difficult to maintain in geological environments because such overpressures can create hydraulic extension fractures and then dissipate (e.g., Byerlee, 1990; Rice, 1992; Sibson, 1996; Faulkner and Rutter, 2001; Healy, 2008; Cox, 2010).

Alternatively, rotation of the principal stresses is possible within and adjacent to fault cores (Faulkner et al., 2006; Healy, 2008). In our three-dimensional stress analysis, rotating the maximum principal stress six degrees counterclockwise towards the fault, to $\sigma_1 = 0/111^\circ$, results in the southern AF being unfavorably, rather than severely, misoriented for slip in fault rocks with 'Byerlee' friction coefficients of $\mu = 0.6$ assuming a stress shape ratio (Φ) of 0.5 (note that the analysis is relatively insensitive to Φ ; cf. Fig. 9). Rotating σ_1 seventeen degrees counterclockwise, to $\sigma_1 = 0/100^\circ$, would make the fault favorably oriented for slip in such materials. Rotations of σ_1 toward the fault are favored by elevated pore fluid pressures within fault zones containing highly anisotropic mineral fabrics and fault parallel fractures (Healy, 2008). There are no constraints on pore fluid pressure or fracture orientation at depth on the southern AF, but detailed cross-sections through surface exposures of the fault zone show that gouge within the core is bounded by anisotropic schist, mylonite, and mélange (Barth et al., 2013).

The paleoseismological record of earthquakes on the AF extends back 8000 years, and accumulating evidence suggests that some ruptures that nucleated on the central AF did not propagate through the southern AF and vice-versa (Wells and Goff, 2007; Clark et al., 2013; Howarth et al., 2016, 2018; Cochran et al., 2017). Given the presence of rate-strengthening gouge with minimum dimensions on the order of 0.012 km wide \times 6 km deep \times 35 km long, the shallow southern AF has the potential to impede earthquake rupture propagation (Figs. 1, 6 and 8) (e.g., Perfettini and Ampuero, 2008; Kaneko et al., 2010; Barbot et al., 2012). According to a simple interpretation of rate-and-state friction, the Earth's crust is composed of three layers: a rate-weakening (negative $a-b$), seismogenic layer, situated between upper (shallow) and lower (deep) rate-strengthening (positive $a-b$) layers prone to aseismic creep (e.g., Marone, 1998). Since aseismic creep relieves tectonic stress, and rate-strengthening material represents an energetic barrier to rupture propagation, shallow and deep portions of crustal faults should arrest earthquake ruptures (Blanpied et al., 1995; Marone, 1998). If the PSS of the southern AF comprises another weak, rate-strengthening mineral(s) at depths greater than ~ 6 km, such as chrysotile or talc (Moore et al., 1997; Moore and Rymer, 2007; Moore and Lockner, 2008), then numerical models indicate that the potential for rupture arrest is linearly proportional to the effective normal stress and along-strike length of the rate-strengthening section (Kaneko et al., 2010; Y. Kaneko, pers. comm., 2017; see also Jolivet et al., 2013).

However, experimental, geodetic, and seismological observations indicate that earthquake ruptures may propagate through rate-strengthening materials because of coseismic slip-induced dynamic weakening (e.g., Di Toro et al., 2011; Ide et al., 2011; Spagnuolo et al., 2016). In contrast to its rate-strengthening behavior at low velocities, water-saturated saponite gouge from Hokuri Creek weakens at

co-seismic slip velocities of 1 m/s, displaying peak and steady state friction coefficients of 0.16 and 0.03, respectively (this study; Boulton et al., 2017b). The low peak and steady-state friction coefficients in the high-velocity experiments can be attributed to thermal pressurization of pore fluids, likely aided by a component of compaction-enhanced pore-fluid pressurization and vaporization (e.g., Ujiie and Tsutsumi, 2010; Ujiie et al., 2011; Faulkner et al., 2011; Chen et al., 2013, 2017; Boulton et al., 2017b). Whether the fault will accelerate enough during an earthquake to activate dynamic weakening mechanisms within the principal slip zone depends primarily on the size of the seismic moment up to that point on the fault, which is determined by the stress drop and area of rate-weakening material that nucleated the rupture and failed dynamically, and on the extent of slip localization (e.g., Rice, 2006; Noda et al., 2009; Noda and Lapusta, 2013). These quantities may differ between earthquake events.

Results from the hydrothermal friction experiments show that saponite fault gouge found along the southern AF is prone to aseismic creep at low velocities. There is sufficient stress to drive slip in the saponite fault gouge, slip along other frictionally weak phyllosilicates (e.g., Moore and Lockner, 2004; Behnsen and Faulkner, 2012), slip in phyllosilicate mixtures deforming by diffusion-assisted pressure-solution creep (Bos and Spiers, 2001, 2002; Jefferies et al., 2006; Richard et al., 2014; Phillips and White, 2017), and slip at the very low apparent friction coefficients observed in all rock types at co-seismic slip rates (Di Toro et al., 2011; Boulton et al., 2017b). Unlike the San Andreas Fault at SAFOD, and many other creeping faults worldwide, there is no geomorphological evidence for shallow creep on the southern AF (Sutherland et al., 2007; Barth et al., 2013, 2014; cf. Harris, 2017). Creeping fault sections often exhibit dense microseismicity, but the seismic network on the southern AF is sparse, with only one recent deployment of 7 seismometers at a spacing of 30–40 km (Warren-Smith et al., 2017b). The recorded seismicity showed that, overall, the southern AF exhibits higher rates of microseismicity than the central AF (e.g., Leitner et al., 2001; Boese et al., 2012; Bourguignon et al., 2015; Warren-Smith et al., 2017b). However, the duration of the recent deployment, along with the seismometer spacing, was insufficient to identify distinct event clusters, accurately constrain shallow hypocentral depths, or to detect very small-magnitude microearthquakes ($M_L < 0.1$) (Warren-Smith et al., 2017b).

The terrain around the southern AF is heavily forested and mountainous, and it contains few man-made features. Because of this, attempts to record active fault creep at the surface by reoccupying old survey networks, generating SAR interferograms, and identifying displaced structures have thus far proved equivocal (e.g., Barth et al., 2013). Fault creep is also spatially and temporally complex; it may occur steadily, seasonally, as episodic transient creep, or as post-seismic afterslip (e.g., Wei et al., 2013; Jolivet et al., 2013; Avouac, 2015). Because the AF is late in its seismic cycle, it is an opportune time to improve the geodetic and seismic networks on the southern AF and use the data to delimit current microseismicity, identify potentially creeping patches, and characterize the nature of the section boundaries near the Martyr River and Puysegur Trench. Improved network coverage will also provide better baseline data on fault slip prior to, during, and after the next plate-boundary earthquake. We posit that, since there is insufficient static stress resolved on the southern AF to shear frictionally strong fault rocks, such rocks, where present, may act as asperities, keeping the fault locked and accumulating stored elastic strain energy. Such asperities may either inhibit or promote rupture propagation depending on the state of stress acting on them prior to and during an earthquake.

5. Conclusions

1. Saponite fault gouge occurs along the southern Alpine Fault for a mapped minimum along-strike distance of 10 km. The fault gouge forms from a serpentinite-rich mélangé that is adjacent to the Alpine

Fault for a minimum strike length of 35 km.

2. A fault gouge containing saponite collected from a 12 m-wide principal slip zone at Hokuri Creek is very weak, with a coefficient of friction of $\mu = 0.12$ – 0.16 across all temperatures ($T = 25$ – 210 °C) and effective normal stresses tested ($\sigma_n' = 31.2$ – 93.6 MPa).
3. The same fault gouge exhibits rate-strengthening (positive α - β) behavior across all temperatures, ($T = 25$ – 210 °C), effective normal stresses ($\sigma_n' = 31.2$ – 93.6 MPa), and velocities ($V = 0.01$ – 3.0 $\mu\text{m/s}$) tested. Rate-strengthening behavior in frictionally weak fault gouge is conducive to aseismic fault creep.
4. The southern Alpine Fault is favorably oriented for slip in saponite fault gouge. Slip in any intact rock or fault gouge with a friction coefficient $\mu \geq 0.5$ would require pore-fluid pressure greater than the least principal stress unless principal stress rotations occur within the fault zone.
5. Insufficient data exist to resolve the presence or absence of active shallow fault creep on the southern Alpine Fault.

Acknowledgements

The U.S. National Earthquake Hazards Reduction Program supported laboratory research. Mark Raven and Lee-Gray Boze are thanked for their technical assistance. This manuscript benefited from discussions with J. Howarth, H. Leclère, Y. Kaneko, and E. Warren-Smith. The Matlab script used for the stress analysis is freely available from H. Leclère. We gratefully acknowledge reviews by N. Beeler, R. Kilgore, R. Harris, and an anonymous reviewer. CB is supported by a Royal Society of New Zealand Rutherford Postdoctoral Fellowship RFT-16-VUW-005-PD and received financial assistance from NERC grant NE/J022128/1. All experimental data are available in the supplementary information and are archived at Boulton et al. (2018). Any use of trade, firm, or product names is for descriptive purposes only and does not imply endorsement by the U.S. Government.

Appendix A. Supplementary data

Supplementary data related to this article can be found at <http://dx.doi.org/10.1016/j.jsg.2018.06.003>.

References

- Ames, L.L., Sand, L.B., 1958. Factors effecting the maximum hydrothermal stability in montmorillonites. *Am. Mineral.* 43, 641–648.
- Anderson, E.M., 1905. The dynamics of faulting. *Trans. Edinb. Geol. Soc.* 8, 387–402.
- Avouac, J.-P., 2015. From geodetic imaging of seismic and aseismic fault slip to dynamic modeling of the seismic cycle. *Annu. Rev. Earth Planet Sci.* 43, 233–271. <https://doi.org/10.1146/annurev-earth-060614-105302>.
- Barnes, P.M., 2009. Postglacial (after 20 ka) dextral slip rate of the offshore Alpine fault, New Zealand. *Geology* 37, 3–6. <https://doi.org/10.1130/B25458>.
- Barnes, P.M., Sutherland, R., Delteil, J., 2005. Strike-slip structure and sedimentary basins of the southern Alpine Fault, Fiordland, New Zealand. *Geol. Soc. Am. Bull.* 117 (3/4), 411–435.
- Barth, N.C., Toy, V.G., Langridge, R.M., Norris, R.J., 2012. Scale dependence of oblique plate-boundary partitioning: new insights from LiDAR, central Alpine fault, New Zealand. *Lithosphere*. <https://doi.org/10.1130/L201.1.L201>.
- Barth, N.C., Boulton, C., Carpenter, B.M., Batt, G.E., Toy, V.G., 2013. Slip localization on the southern Alpine Fault, New Zealand. *Tectonics* 32, 620–640. <https://doi.org/10.1002/tect.20041>.
- Barth, N.C., Kulhanek, D.K., Beu, A.G., Murray-Wallace, C.V., Hayward, B.W., Mildenhall, D.C., Lee, D.E., 2014. New c. 270 kyr strike-slip and uplift rates for the southern Alpine Fault and implications for the New Zealand plate boundary. *J. Struct. Geol.* 64, 39–52. <https://doi.org/10.1016/j.jsg.2013.08.009>.
- Barbot, S., Lapusta, N., Avouac, J.-P., 2012. Under the hood of the earthquake machine: toward predictive modeling of the seismic cycle. *Science* 336, 707–710.
- Beavan, J., Moore, M., Pearson, C., Henderson, M., et al., 1999. Crustal deformation during 1994–1998 due to oblique continental collision in the central Southern Alps, New Zealand, and implications for seismic potential of the Alpine fault. *J. Geophys. Res.* 104 (B11), 25,233–25,255.
- Beavan, J., Denys, P., Denham, M., Hager, B., Herring, T., Molnar, P., 2010. Distribution of present-day vertical deformation across the Southern Alps, New Zealand, from 10 years of GPS data. *Geophys. Res. Lett.* 37, L16305. <http://dx.doi.org/10.1029/2010GL044165>.
- Behnsen, J., Faulkner, D.R., 2012. The effect of mineralogy and effective normal stress on frictional strength of sheet silicates. *J. Struct. Geol.* 42, 49–61. <https://doi.org/10.1016/j.jsg.2012.06.015>.

- Berryman, K., Beanland, S., Cooper, A., Cutten, H., Norris, R., Wood, P., 1992. The Alpine Fault, New Zealand: variation in Quaternary structural style and geomorphic expression. *Ann. Tect.* **IV**, 126–163.
- Berryman, K.B., Cochran, U.A., Clark, K.J., Biasi, G.P., Langridge, R.M., Villamor, P., 2012. Major earthquakes occur regularly on an isolated plate boundary fault. *Science* **29** (336), 1690–1693. <https://doi.org/10.1126/science.1218959>.
- Blanpied, M.L., Lockner, D.A., Byerlee, J.D., 1995. Frictional slip of granite at hydrothermal conditions. *J. Geophys. Res.* **100**, 13045–13064.
- Boese, C.M., 2012. Microseismicity in the central Southern Alps, Westland, New Zealand. PhD Thesis. Victoria University of Wellington, New Zealand.
- Boese, C.M., Townend, J., Smith, E., Stern, T., 2012. Microseismicity and stress in the vicinity of the Alpine Fault, central southern alps, New Zealand. *J. Geophys. Res.* **117** B02302 <http://dx.doi.org/10.1029/2011JB008460>.
- Boese, C.M., Stern, T.A., Townend, J., Bourgiugnon, S., Sheehan, A., Smith, E.G.C., 2013. Sub-crustal earthquakes within the Australia-Pacific plate boundary zone beneath the Southern Alps, New Zealand. *Earth Planet. Sci. Lett.* <https://doi.org/10.1016/j.epsl.2013.06.030>.
- Boles, A., Mulch, A., van der Pluijm, B., 2018. Near-surface clay authigenesis in exhumed fault rock of the Alpine Fault Zone (New Zealand); O-H-Ar isotopic, XRD and chemical analysis of illite and chlorite. *J. Struct. Geol.* **111**, 27–41.
- Bos, B., Spiers, C.J., 2001. Experimental investigation into the microstructural and mechanical evolution of phyllosilicate-bearing fault rock under conditions favouring pressure solution. *J. Struct. Geol.* **23**, 1187–1202.
- Bos, B., Spiers, C.J., 2002. Frictional-viscous flow of phyllosilicate-bearing fault rock: microphysical model and implications for crustal strength profiles. *J. Geophys. Res.* **107**. <https://doi.org/10.1029/2001JB003011>.
- Bott, M.H.P., 1959a. The mechanics of oblique slip faulting. *Geol. Mag.* **96** (2), 109–117.
- Bourgiugnon, S., Bannister, S., Mark Henderson, C., Townend, J., Zhang, H., 2015. Structural heterogeneity of the midcrust adjacent to the central Alpine Fault, New Zealand: inference from seismic tomography and seismicity between Harihari and Ross. *Geochim. Geophys. Geosys.* **16**, 1017–1043. <https://doi.org/10.1002/2014GC005702>.
- Boulton, C., 2013. Experimental Investigation of Gouges and Cataclases, Alpine Fault, New Zealand. PhD Thesis. University of Canterbury. <http://hdl.handle.net/10092/8917>.
- Boulton, C., Carpenter, B.M., Toy, V.G., Marone, C., 2012. Physical properties of surface outcrop cataclastic fault rocks, Alpine Fault, New Zealand. *Geochim. Geophys. Geosys.* **13**. <https://doi.org/10.1029/2011GC003872>.
- Boulton, C., Moore, D.E., Lockner, D.A., Toy, V.G., Townend, J., Sutherland, R., 2014. Frictional properties of exhumed fault gouges in DFDP-1 cores, Alpine Fault, New Zealand. *Geophys. Res. Lett.* **41**. <https://doi.org/10.1002/2013GL058236>.
- Boulton, C., Menzies, C.D., Toy, V.G., Townend, J., Sutherland, R., 2017a. Geochemical and microstructural evidence for interseismic changes in fault zone permeability and strength, Alpine Fault, New Zealand. *Geochim. Geophys. Geosyst.* **18**. <https://doi.org/10.1002/2016GC006588>.
- Boulton, C., Yao, L., Faulkner, D.R., Townend, J., Toy, V.G., Sutherland, R., Ma, S., Shimamoto, T., 2017b. High-velocity frictional properties of Alpine Fault rocks: mechanical data, microstructural analysis, and implications for rupture propagation. *J. Struct. Geol.* **97**, 71–92. <https://doi.org/10.1016/j.jsg.2017.02.003>.
- Boulton, C., Barth, N., Moore, D.E., Lockner, D.A., Townend, J., Faulkner, D.R., 2018. Data for Frictional Properties and 3-D Stress Analysis of the Southern Alpine Fault. <http://dx.doi.org/10.5066/P9PPLQJM>. New Zealand: U.S. Geological Survey data release.
- Bradbury, K.K., Evans, J.P., Chester, J.S., Chester, F.M., Kirschner, D.L., 2011. Lithology and internal structure of the San Andreas fault at depth based on characterization of Phase 3 whole-rock core in the San Andreas Fault Observatory at Depth (SAFOD) borehole. *Earth Planet. Sci. Lett.* **310**, 131–144. <https://doi.org/10.1016/j.epsl.2011.07.020>.
- Byerlee, J., 1978. Friction of rocks. *Pure Appl. Geophys.* **116**, 615–626.
- Byerlee, J., 1990. Friction, overpressure and fault normal compression. *Geophys. Res. Lett.* **17** (12), 2109–2112.
- Carpenter, B.M., Saffer, D.M., Marone, C., 2012. Frictional properties and sliding stability of the San Andreas Fault from deep drill core. *Geology* **40** (8), 759–762. <https://doi.org/10.1130/G33007.1>.
- Carpenter, B.M., Saffer, D.M., Marone, C., 2015. Frictional properties of the active San Andreas Fault at SAFOD: implications for fault strength and slip behavior. *J. Geophys. Res.* **120**, 5273–5289. <https://doi.org/10.1002/2015JB011963>.
- Chen, J., Yang, X., Duan, Q., Shimamoto, T., Spiers, C.J., 2013. Importance of thermochemical pressurization in the dynamic weakening of the Longmenshan Fault during the 2008 Wenchuan earthquake: inferences from experiments and modeling. *J. Geophys. Res. Solid Earth* **118**, 1–25. <https://doi.org/10.1002/jgrb.50260>.
- Chen, J., Niemeijer, A., Yao, L., Ma, S., 2017. Water vaporization promotes coseismic fluid pressurization and buffers temperature rise. *Geophys. Res. Lett.* **44**, 2177–2185. <https://doi.org/10.1002/2016GL071932>.
- Clark, K.J., Cochran, U.A., Berryman, K.R., Biasi, G., Langridge, R., Villamor, P., Bartholomew, T., Litchfield, N., Pantosi, D., Marco, S., Van Dissen, R., Turner, G., Hemphill-Haley, M., 2013. Deriving a long paleoseismic record from a shallow-water Holocene basin next to the Alpine fault, New Zealand. *Geol. Soc. Am. Bull.* **125** (5–6), 811–832.
- Coble, C.G., French, M.E., Chester, F.M., Chester, J.S., Kitajima, H., 2014. In situ frictional properties of San Andreas Fault gouge at SAFOD. *Geophys. J. Int.* **199**, 956–967.
- Cochran, U.A., Clark, K.J., Howarth, J.D., Biasi, G.P., Langridge, R.M., Villamor, P., Berryman, K.R., Vandergoes, M.J., 2017. A plate boundary earthquake record from a wetland adjacent to the Alpine fault in New Zealand refines hazard estimates. *Earth Planet. Sci. Lett.* **464**, 175–188.
- Cooper, A.F., Norris, R.J., 1994. Anatomy, structural evolution and slip rate of a plate-boundary thrust: the Alpine fault at Gaunt Creek, Westland, New Zealand. *Geol. Soc. Am. Bull.* **106**, 627–633.
- Cox, S.F., 2010. The application of failure mode diagrams for exploring the roles of fluid pressure and stress states in controlling styles of fracture-controlled permeability enhancement in faults and shear zones. *Geofluids* **10**, 217–233. <https://doi.org/10.1111/j.1468-8123.2010.00281.x>.
- DeMets, C., Gordon, R.G., Argus, D.F., Stein, S., 1994. Effect of revision to the geomagnetic reversal time scale on estimates of current plate motions. *Geophys. Res. Lett.* **21**, 2191–2194. <https://doi.org/10.1029/94GL02118>.
- Dieterich, J.H., 1979. Modeling of rock friction 1. Experimental results and constitutive equations. *J. Geophys. Res.* **84** (B5), 2162–2168. <https://doi.org/10.1029/JB084iB05p02151>.
- Di Toro, G., Han, R., Hirose, T., De Paola, N., Nielsen, S., Mizoguchi, K., Ferri, F., Cocco, M., Shimamoto, T., 2011. Fault lubrication during earthquakes. *Nature* **471**, 494–499. <https://doi.org/10.1038/nature09838>.
- Eberl, E., Whitney, G., Khoury, H., 1978. Hydrothermal reactivity of smectite. *Am. Mineral.* **63**, 401–409.
- Evison, F.F., 1971. Seismicity of the Alpine Fault, New Zealand. *Recent crustal movements. R. Soc. N. Z. Bull.* **9**, 161–165.
- Faulkner, D.R., Rutter, E.H., 2001. Can the maintenance of overpressured fluids in large strike-slip fault zones explain their apparent weakness? *Geology* **29** (6), 503–506.
- Faulkner, D.R., Mitchell, T.M., Healy, D., Heap, M.J., 2006. Slip on ‘weak’ faults by the rotation of regional stress in the fracture damage zone. *Nature* **444** (7121), 922–925.
- Faulkner, D.R., Jackson, C.A.L., Lunn, R.J., Schlichte, R.W., Shipton, Z.K., Wibberley, C.A.J., Withjack, M.O., 2010. A review of recent developments concerning the structure, mechanics and fluid flow properties of fault zones. *J. Struct. Geol.* **32** (11), 1557–1575. <https://doi.org/10.1016/j.jsg.2010.06.009>.
- Faulkner, D.R., Mitchell, T.M., Behnsen, J., Hirose, T., Shimamoto, T., 2011. Stuck in the mud? Earthquake nucleation and propagation through accretionary forearcs. *Geophys. Res. Lett.* **38**. <https://doi.org/10.1039/2011GL048552>.
- Faulkner, D.R., Sanchez-Roa, C., Boulton, C., den Hartog, S.A.M., 2018. Pore-fluid pressure development in compacting fault gouge in theory, experiments, and nature. *J. Geophys. Res. Solid Earth*. <https://doi.org/10.1002/2017JB015130>.
- French, M.E., Chester, J.S., Chester, F.M., 2015. Micromechanisms of creep in clay-rich gouge from the central deforming zone of the San Andreas Fault. *J. Geophys. Res.* **120**, 827–849. <https://doi.org/10.1002/2014JB011496>.
- Harris, R.A., 2004. Numerical simulations of large earthquakes: dynamic rupture propagation on heterogeneous faults. *Pure Appl. Geophys.* **161**, 2171–2181.
- Harris, R.A., 2017. Large earthquakes and creeping faults. *Rev. Geophys.* **55**, 169–198. <https://doi.org/10.1002/2016RG000539>.
- Healy, D., 2008. Damage patterns, stress rotations and pore fluid pressures in strike-slip fault zones. *J. Geophys. Res.* **113** B12407. <https://doi.org/10.1029/2008JB005655>.
- Holdsworth, R.E., van Diggelen, E.W.E., Spiers, C.J., de Bresser, J.H.P., Walker, R.J., Bowen, L., 2011. Fault rock samples from the SAFOD core samples: implications for weakening at shallow depths along the San Andreas Fault, California. *J. Struct. Geol.* **33**, 132–144.
- Howarth, J., Fitzsimons, S.J., Norris, R.J., Jacobsen, G.E., 2012. Lake sediments record cycles of sediment flux driven by large earthquakes on the Alpine Fault, New Zealand. *Geology* **40**, 1091–1094. <https://doi.org/10.1130/G33486.1>.
- Howarth, J.D., Fitzsimons, S.J., Norris, R.J., Langridge, R., Vandergoes, M.J., 2016. A 2000 yr rupture history for the Alpine Fault derived from lake Ellery, South Island, New Zealand. *Geol. Soc. Am. Bull.* **128** (3/4), 627–642. <https://doi.org/10.1130/B31300.1>.
- Howarth, J.D., Cochran, U.A., Langridge, R.M., Clark, K., Fitzsimons, S.J., Berryman, K., Villamor, P., Strong, D.T., 2018. Past large earthquakes on the Alpine Fault: paleoseismological progress and future directions. *N. Z. J. Geol. Geophys.* <https://doi.org/10.1080/00288306.2018.1464658>.
- Ide, S., Baltay, A., Beroza, G.C., 2011. Shallow dynamic overshoot and energetic deep rupture in the 2011 M_w 9.0 Tohoku-Oki earthquake. *Science* **332**, 1426–1428.
- Ikari, M.J., Trütnner, S., Carpenter, B.M., Kopf, A.J., 2015. Shear behavior of DFDP-1 borehole samples from the Alpine Fault, New Zealand, under a wide range of experimental conditions. *Int. J. Earth Sci.* **104** (6), 1523–1535.
- Jaeger, J.C., Cook, N.G.W., Zimmerman, R., 2007. *Fundamentals of Rock Mechanics*, fourth ed. Blackwell, Oxford, pp. 475.
- Jefferies, S.P., Holdsworth, R.E., Shimamoto, T., Takagi, H., Lloyd, G.E., Spiers, C.J., 2006. Origin and mechanical significance of foliated cataclastic rocks in the cores of crustal-scale faults: Examples from the Median Tectonic Line, Japan. *J. Geophys. Res.* **111** B12303. <https://doi.org/10.1029/2005JB004205>.
- Jolivet, R., Simon, M., Agram, P.S., Duputel, Z., Shen, Z.-K., 2015. Aseismic slip and seismicogenic coupling along the central San Andreas Fault. *Geophys. Res. Lett.* **42**, 297–306. <https://doi.org/10.1002/2014GL062222>.
- Jolivet, R., Lasserre, C., Doi, M.-P., Peltzer, G., Avouac, J.-P., Sun, J., Dailu, R., 2013. Spatio-temporal evolution of aseismic slip along the Haiyuan fault, China: implications for fault frictional properties. *Earth Planet. Sci. Lett.* **377**–378, 23–33.
- Kaduri, M., Gratier, J.-P., Renard, F., Çakır, Z., Lasserre, C., 2017. The implications of fault zone transformation on aseismic creep: example of the North Anatolian Fault, Turkey. *J. Geophys. Res. Solid Earth* **122**, 4208–4236. <https://doi.org/10.1002/2016JB013803>.
- Kaneko, Y., Avouac, J.-P., Lapusta, N., 2010. Towards inferring earthquake patterns from geodetic observations of interseismic coupling. *Nat. Geosci.* **3**, 363–369. <https://doi.org/10.1038/NGE0843>.
- King, G., 1986. Speculations on the geometry of the initiation and termination process of earthquake rupture and its relation to morphology and geological structure. *Pure Appl. Geophys.* **124**, 567–585.
- Klopprogge, J.T., Komarneni, S., Amonette, J.E., 1999. Synthesis of smectite clay minerals: a critical review. *Clay Clay Miner.* **47** (5), 529–554.
- Koons, P.O., 1987. Some thermal and mechanical consequences of rapid uplift: an example from the Southern Alps, New Zealand. *Earth Planet. Sci. Lett.* **86**, 307–319.
- Lamb, S., Smith, E., Stern, T., Warren-Smith, E., 2015. Continental-scale strike-slip on a low-angle fault beneath New Zealand's Southern Alps: implications for crustal thickening in oblique collision zones. *Geochim. Geophys. Geosyst.* **16**. <https://doi.org/10.1002/2015GC005990>.
- Leclère, H., Fabbri, O., 2013. A new three-dimension method of fault reactivation analysis. *J. Struct. Geol.* **48**, 153–161. <https://doi.org/10.1016/j.jsg.2012.11.004>.

- Leclère, H., Daniel, G., Fabbri, O., Cappa, F., Thouvenot, F., 2013. Tracking fluid pressure buildup from focal mechanisms during the 2003–2004 Ubaye seismic swarm, France. *J. Geophys. Res. Solid Earth* 118, 4461–4476. <https://doi.org/10.1002/jgrb.50297>.
- Leitner, B., Eberhart-Phillips, D., Anderson, H., Nabelek, J.L., 2001. A focused look at the Alpine fault, New Zealand: seismicity, focal mechanisms, and stress observations. *J. Geophys. Res.* 106 (B2), 2193–2220.
- Little, T.A., Cox, S., Vry, J.K., Batt, G., 2005. Variations in exhumation level and uplift rate along the oblique-slip Alpine fault, central Southern Alps, New Zealand. *Geol. Soc. Am. Bull.* 117 (5–6), 707–723.
- Lockner, D.A., Morrow, C., Moore, D., Hickman, S., 2011. Low strength of deep San Andreas Fault gouge from SAFOD core. *Nature* 472, 82–85. <https://doi.org/10.1038/nature09927>.
- Marone, C., 1998. Laboratory-derived friction laws and their application to seismic faulting. *Annu. Rev. Earth Planet Sci.* 26, 643–696.
- Massiot, C., Celerier, B., Doan, M.-L., et al., 2018. The Alpine Fault hanging wall viewed from within: structural analysis of ultrasonic image logs in the DFDP-2B borehole, New Zealand. *Geochem. Geophys. Geosyst.* <https://doi.org/10.1029/2017GC007368>.
- Meunier, A., 2005. *Clays*. Springer-Verlag, Berlin Heidelberg, pp. 472.
- Moore, D.E., 2014. Comparative mineral chemistry and textures of SAFOD fault gouge and damage-zone rocks. *J. Struct. Geol.* 68, 82–96. <https://doi.org/10.1016/j.jsg.2014.09.002>.
- Moore, D.E., Lockner, D.A., 2011. Frictional strengths of talc-serpentine and talc-quartz mixtures. *J. Geophys. Res.* 116 (B01403). <https://doi.org/10.1029/2010JB007881>.
- Moore, D.E., Lockner, D.A., 2008. Talc friction in the temperature range 25–400°C: Relevance for fault-zone weakening. *Tectonophysics* 449, 120–132.
- Moore, D.E., Lockner, D.A., 2004. Crystallographic controls on the frictional behavior of dry and water-saturated sheet-structure minerals. *J. Geophys. Res.* 109, B03401. <https://doi.org/10.1029/2003JB002582>.
- Moore, D.E., Rymer, M.J., 2007. Talc-bearing serpentinite and the creeping section of the San Andreas fault. *Nature* 448, 795–797.
- Moore, D.E., Lockner, D.A., Hickman, S., 2016. Hydrothermal frictional strengths of rock and mineral samples relevant to the creeping section of the San Andreas Fault. *J. Struct. Geol.* 89, 153–167.
- Moore, D.E., Lockner, D.A., Shengli, M., Summers, R., Byerlee, J.D., 1997. Strengths of serpentinite gouges at elevated temperatures. *J. Geophys. Res.* 102 (B7), 14787–14801. <https://doi.org/10.1029/97JB00995>.
- Morris, A., Ferrill, D.A., Henderson, D.B., 1996. Slip-tendency analysis and fault reactivation. *Geology* 24, 275–278.
- Morrow, C.A., Moore, D.E., Lockner, D.A., 2017. Frictional strength of wet and dry montmorillonite. *J. Geophys. Res. Solid Earth* 122, 3392–3409. <http://dx.doi.org/10.1002/2016JB013658>.
- Nevis, M., Paiva, L., Luis, J., 2009. Software for slip-tendency analysis in 3D: a plug-in for Coulomb. *Comput. Geosci.* 35, 2345–2352.
- Niemeijer, A.R., Boulton, C., Toy, V.G., Townend, J., Sutherland, R., 2016. Large-displacement, hydrothermal frictional properties of DFDP-1 fault rocks, Alpine Fault, New Zealand: implications for deep rupture propagation. *J. Geophys. Res. Solid Earth* 121. <https://doi.org/10.1002/2015JB012593>.
- Noda, H., Lapusta, N., 2013. Stable creeping fault segments can become destructive as a result of dynamic weakening. *Nature*. <https://doi.org/10.1038/nature11703>.
- Noda, H., Dunham, E.M., Rice, J.R., 2009. Earthquake ruptures with thermal weakening and the operation of major faults at low overall stress levels. *J. Geophys. Res.* 114 (B07302). <https://doi.org/10.1029/2008JB006143>.
- Norris, R.J., Cooper, A.F., 2001. Late Quaternary slip rates and slip partitioning on the Alpine fault, New Zealand. *J. Struct. Geol.* 23, 507–520. [https://doi.org/10.1016/S0191-8141\(00\)00122-X](https://doi.org/10.1016/S0191-8141(00)00122-X).
- Norris, R.J., Cooper, A.F., 2007. The Alpine Fault, New Zealand: surface geology and field relationships. In: In: Okaya, D., Stern, T., Davey, F. (Eds.), *A Continental Plate Boundary: Tectonics at South Island, New Zealand*, Geophys. Monogr. Ser. vol. 175. AGU, Washington, D.C, pp. 159–178.
- Perfettini, H., Ampuero, J.-P., 2008. Dynamics of a velocity strengthening region: implications for slow earthquakes and postseismic slip. *J. Geophys. Res.* 113 (B9), B09317. <https://doi.org/10.1029/2007JB005398>.
- Phillips, N.J., White, J.C.W., 2017. Grain size-dependent strength of phyllosilicate-rich gouges in the shallow crust: insights from the SAFOD site. *J. Geophys. Res. Solid Earth* 122, 5789–5812. <https://doi.org/10.1002/2016JB013828>.
- Rice, J.R., 1992. Fault stress states, pore pressure distributions, and the weakness of the San Andreas fault. In: Evans, B., Wong, T.-F. (Eds.), *Fault Mechanics and Transport Properties of Rocks*. Academic Press Ltd., New York, pp. 475–503.
- Rice, J.R., 2006. Heating and weakening of faults during earthquake slip. *J. Geophys. Res.* 111, B05311. <https://doi.org/10.1029/2005JB004006>.
- Richard, J., Gratier, J.-P., Doan, M.-L., Boullier, A.-M., Renard, F., 2014. Rock and mineral transformations in a fault zone leading to permanent creep: interactions between brittle and viscous mechanisms in the San Andreas Fault. *J. Geophys. Res. Solid Earth* 119. <https://doi.org/10.1002/2014JB011489>.
- Ruina, A.L., 1983. Slip instability and state variable friction laws. *J. Geophys. Res.* 88 (B12), 10359–10370. <https://doi.org/10.1029/JB088iB12p10359>.
- Saffer, D.M., Marone, C., 2003. Comparison of smectite- and illite-rich gouge frictional properties: application to the updip limit of the seismogenic zone along subduction megathrusts. *Earth Planet. Sci. Lett.* 215, 219–235.
- Schleicher, A.M., van der Pluijm, B.A., Warr, L.M., 2012. Chlorite-smectite clay minerals and fault behavior: new evidence from the San Andreas Fault observatory at depth (SAFOD) core. *Lithosphere* 4 (3), 209–220. <https://doi.org/10.1130/L158.1>.
- Sibson, R.H., 1985. A note on fault reactivation. *J. Struct. Geol.* 7 (6), 751–754.
- Sibson, R.H., 1996. Structural permeability of fluid-driven fault-fracture meshes. *J. Struct. Geol.* 18 (8), 1031–1042.
- Sone, H., Shimamoto, T., Moore, D.E., 2012. Frictional properties of a metasomatic saponite-rich gouge from a serpentinite-bearing fault zone in the Gokasho-Arashima Tectonic Line, central Japan. *J. Struct. Geol.* 38, 172–182. <https://doi.org/10.1016/j.jsg.2011.09.007>.
- Spagnuolo, E., Nielsen, S., Violay, M., Di Toro, G., 2016. An empirically based steady state friction law and implications for fault stability. *Geophys. Res. Lett.* 43, 3263–3271. <https://doi.org/10.1002/2016GL067881>.
- Stirling, M.W., McVerry, G.H., Gerstenberger, M., et al., 2012. National seismic hazard model for New Zealand: 2010 update. *Bull. Seismol. Soc. Am.* 102 (4), 1514–1542.
- Sutherland, R., Davey, F., Beavan, J.P., 2000. Plate boundary deformation in South Island, New Zealand, is related to inherited lithospheric structure. *Earth Planet. Sci. Lett.* 177, 141–151.
- Sutherland, R., et al., 2007. Do great earthquakes occur on the Alpine fault in central South Island, New Zealand? In: In: Okaya, D. (Ed.), *A Continental Plate Boundary: Tectonics at South Island, New Zealand*, Geophysical Monograph, vol. 175. American Geophysical Union, pp. 235–251.
- Sutherland, R., et al., 2012. Drilling reveals fluid control on architecture and rupture of the Alpine Fault, New Zealand. *Geology* 40, 1143–1146. <https://doi.org/10.1130/G33614.1>.
- Sutherland, R., et al., 2017. Extreme hydrothermal conditions at an active plate-bounding fault. *Nature* 546, 137–141.
- Tembe, S., Lockner, D.A., Wong, T.F., 2010. Effect of clay content and mineralogy on frictional sliding behavior of simulated gouges: binary and ternary mixtures of quartz, illite, and montmorillonite. *J. Geophys. Res.* 115, B03416. <https://doi.org/10.1029/2009JB006383>.
- Titus, S.J., DeMets, C., Tikoff, B., 2006. Thirty-five-year creep rates for the creeping segment of the San Andreas Fault and the effects of the 2004 Parkfield earthquake: constraints from alignment arrays, continuous global positioning system, and creepmeters. *Bull. Seismol. Soc. Am.* 96 (4B), S250–S268. <https://doi.org/10.1029/2005JB006383>.
- Townend, J., 1999. Heat flow through the west Coast, South Island, New Zealand. *N. Z. Geol. Geophys.* 42 (1), 21–31.
- Townend, J., Sutherland, R., Toy, V.G., 2009. Deep Fault drilling Project-Alpine Fault, New Zealand. *Sci. Drill.* 8, 75–82.
- Townend, J., Sherburn, S., Arnold, R., Boese, C., Woods, L., 2012. Three-dimensional variations in present-day tectonic stress along the Australia-Pacific plate boundary in New Zealand. *Earth Planet. Sci. Lett.* 353–354, 47–59.
- Townend, J., Sutherland, R., Toy, V.G., et al., 2017. Petrophysical, geochemical, and hydrological evidence for extensive fracture-mediated fluid and heat transport in the Alpine Fault's hanging-wall damage zone. *Geochem. Geophys. Geosyst.* <https://doi.org/10.1002/2017GC007202>.
- Ujii, K., Tsutsumi, A., 2010. High-velocity frictional properties of clay-rich fault gouge in a megaslip fault zone, Nakai subduction zone. *Geophys. Res. Lett.* 37, L24310. <https://doi.org/10.1029/2010GL046002>.
- Ujii, K., Tsutsumi, A., Kameda, J., 2011. Reproduction of thermal pressurization and fluidization of clay-rich fault gouges by high-velocity friction experiments and implications for seismic slip in natural faults. In: In: Fagereng, Å., Toy, V.G., Rowland, J.V. (Eds.), *Geology of the Earthquake Source: a Volume in Honour of Rick Sibson*, vol. 359. Geol. Soc. London Special Pub, pp. 267–285.
- Upton, P., Song, B.R., Koons, P.O., 2018. Topographic control on shallow fault structure and strain partitioning near Whataroa, New Zealand, demonstrates weak Alpine Fault. *N. Z. J. Geol. Geophys.* 61 (1), 1–8. <https://doi.org/10.1080/00288306.2017.1397706>.
- Velde, B., Meunier, A., 2008. *The Origin of Clay Minerals in Soils and Weathered Rocks*. Springer-Verlag, Berlin Heidelberg, pp. 406.
- Warr, L.N., Cox, S., 2001. Clay mineral transformations and weakening mechanisms along the Alpine Fault, New Zealand. In: In: Holdsworth, R.E., Strachan, R.A., Magloughlin, J.F., Knipe, R.J. (Eds.), *The Nature and Tectonic Significance of Fault Zone Weakening*, vol. 186. Geol. Soc. London Spec. Pub, pp. 85–101.
- Warren-Smith, E., Lamb, S., Stern, T.A., 2017a. Stress field and kinematics for diffuse microseismicity in a zone of continental transpression, South Island, New Zealand. *J. Geophys. Res. Solid Earth* 122. <https://doi.org/10.1002/2017JB013942>.
- Warren-Smith, E., Lamb, S., Stern, T.A., Smith, E., 2017b. Microseismicity in southern South Island, New Zealand: implications for the mechanism of crustal deformation adjacent to a major continental transform. *J. Geophys. Res. Solid Earth.* <https://doi.org/10.1002/2017JB013942>.
- Wellman, H.W., 1953. Data for the study of recent and late Pleistocene faulting in the South Island of New Zealand. *N. Z. J. Sci. Technol.* 34B, 270–288.
- Wells, A., Goff, J., 2007. Coastal dunes in Westland, New Zealand, provide a record of paleoseismic activity on the Alpine fault. *Geology* 35 (8), 731–734. <https://doi.org/10.1130/G23554A.1>.
- Wells, A., Yettton, M.D., Duncan, R.P., Stewart, G.H., 1999. Prehistoric dates of the most recent Alpine Fault earthquakes, New Zealand. *Geology* 27 (11), 995–998.
- Wesnousky, S.G., 1988. Seismological and structural evolution of strike-slip faults. *Nature* 335, 340–342.
- Wei, M., Kaneko, Y., Liu, Y., McGuire, J., 2013. Episodic fault creep events in California controlled by shallow frictional heterogeneity. *Nat. Geosci.* 6, 566–570. <https://doi.org/10.1038/NGEO1835>.